Supplementary Information (SI) for Journal of Materials Chemistry A.
This journal is © The Royal Society of Chemistry 2026

Supplementary Material

Dual-site cationic disorder engineering for ultralow amorphous-like thermal conductivity in thermal barrier coatings

Zide Wu [a], *Yuning Cao* [a], *Jiaxin Xue* [a], *Tianyixiao Yang* [a], *Zhiyuan Ma* [b], *Mu Li* [a] *, *Dawei Tang* [a]

[a] Key Laboratory of Ocean Energy Utilization and Energy Conservation of Ministry of Education, School of Energy and Power Engineering, Dalian University of Technology, Dalian, 116024, China

[b] NDT & E Laboratory, Dalian University of Technology, Dalian, 116024, China

* Corresponding author. limu@dlut.edu.cn

1. Characterization

1.1 Phase composition and microstructure

The phase compositions of the synthesized samples were characterized by X-ray diffraction (XRD, X'per, PANalytical) using Cu Kα radiation. Data were collected in the 2θ range from 10° to 90° with a step size of 0.013° and a scanning rate of 0.0417 ° s^{-1}. Rietveld refinement of the XRD data was performed using the commercial software GSAS-II to determine the crystal structural parameters.

The microstructure and elemental distribution of the sintered pellets were examined using a field emission scanning electron microscope (FE-SEM, SU5000, Hitachi) equipped with an energy dispersive X-ray spectrometer (EDS, Ultim Max, Oxford). The chemical states of oxygen and doping cations were analyzed by X-ray photoelectron spectroscopy (XPS, K-Alpha, Thermo Fisher).

1.2 Thermophysical properties

The thermal diffusivity (λ) was measured from 300 K to 1300 K under an argon atmosphere using a laser flash analyzer (LFA, LFA 467, NETZSCH). Both surfaces of the samples were coated with a thin layer of graphite to ensure complete and uniform absorption of the laser pulse and consistent surface emissivity. Meanwhile, the specific heat capacity (C_p) was estimated based on the Neumann-Kopp rule. The bulk density (ρ) was determined by the Archimedes method. Finally, the thermal conductivity (κ) was calculated using the following formula:

$$\kappa = \lambda \cdot C_p \cdot \rho \tag{1}$$

Finally, the intrinsic thermal conductivity of the fully dense sample (κ') was corrected from the measured value κ with φ:

$$\frac{\kappa}{\kappa'} = 1 - \frac{4}{3}\varphi \tag{2}$$

On the other hand, the thermal expansion behavior was measured using a thermal dilatometer (TEC, DIL 402, NETZSCH) from 300 K to 1300 K under a flowing argon atmosphere at a constant heating rate of 5 K min^{-1}. The thermal expansion coefficient (α) at different temperature was calculated as:

$$\alpha = \frac{dL}{(T - T_0)L_0} \tag{3}$$

where L_0 and dL represent the original length at the initial temperature T_0 and its change in length at temperature T respectively.

1.3 Mechanical properties

The elastic properties of the synthesized samples were determined by the ultrasonic reflection method. Ultrasonic waves were generated by a computer-controlled pulser/receiver (Model 5800, Olympus). A 10 MHz longitudinal wave transducer and a transverse wave transducer were employed to obtain the waveform signals, which were captured by a digital phosphor oscilloscope. The time difference between the first and the second back-wall echoes was used to calculate the longitudinal (V_L) and transverse (V_T) acoustic velocities.

The mean acoustic velocity (V_M), Young's modulus (E), Poisson's ratio (v), Bulk modulus (B) and shear modulus (G) were calculated using V_L and V_T with the following equations:

$$V_M = \left[\frac{1}{3}\left(\frac{1}{V_L^3} + \frac{2}{V_T^3}\right)\right]^{-\frac{1}{3}} \tag{4}$$

$$E = \frac{\rho V_L^2 \left(3V_L^2 - 4V_T^2\right)}{\left(V_L^2 - V_T^2\right)} \tag{5}$$

$$\upsilon = \frac{1-2\left(\frac{V_T}{V_L}\right)^2}{2-2\left(\frac{V_T}{V_L}\right)^2} \tag{6}$$

$$B = \frac{E}{3(1-2\nu)} \tag{7}$$

$$G = \frac{E}{2(1+\nu)} \tag{8}$$

In addition, the Vickers hardness (H_V) of the samples was measured using a Vickers harness tester (HRS-150, Shangcai) with a load of 500 N and a dwell time of 10 s. The fracture toughness (K_{IC}) was subsequently calculated as follows:

$$K_{IC} = 0.16 H_V a^{0.5} \left(\frac{c}{a}\right)^{-1.5} \tag{9}$$

where a and c denote the average length of the Vickers indentation diagonal, and the crack length, respectively.

2. Phase stability of $La_{1-x}Y_x$-HE

Fig. S1 illustrates the Rietveld refinement of XRD patterns for LZO and $La_{1-x}Y_x$-HE. For $x \leq 0.5$, the pyrochlore model was employed for refinements; while for $x > 0.5$, the defect fluorite model was used. All samples exhibit R_{wp} values below 5%, indicating that the structural models are reliable. With B-site high-entropy doping, the lattice parameter of $La_{1.000}Y_{0.000}$-HE increased from 10.81 Å (LZO) to 10.87 Å ($La_{1.000}Y_{0.000}$-HE). As the A-site Y^{3+} content increases, the lattice parameter gradually decreased, reaching 10.69 Å for $La_{0.500}Y_{0.500}$-HE. Subsequently, the composition transformed into the defect-fluorite phase, with lattice parameters of 5.31 Å and 5.30 Å for $La_{0.375}Y_{0.625}$-HE and $La_{0.250}Y_{0.750}$-HE, respectively.

Second, to verify the validity of the simultaneous *A*-site and *B*-site cooping of Y^{3+} in our model, we conducted the following supplementary validations. Quantitative Rietveld refinements were utilized to further exclude the possibility of single-site occupancy for Y^{3+}. To prove this, we constructed and evaluated four hypothetical models where Y^{3+} exclusively occupies the *B* site: $(La_{0.500}Ce_{0.125}Sn_{0.125}Zr_{0.250})_2(Nb_{0.250}Y_{0.750})_2O_7$, $(La_{0.500}Ce_{0.125}Sn_{0.125}Nb_{0.250})_2(Zr_{0.250}Y_{0.750})_2O_7$, $(La_{0.500}$-$Nb_{0.250}Zr_{0.250})_2(Ce_{0.125}Sn_{0.125}Y_{0.750})_2O_7$, and where Y^{3+} occupies only the *A* site: $(La_{0.250}Y_{0.750})_2$-$(Zr_{0.250}Ce_{0.125}Sn_{0.125}Nb_{0.250}La_{0.250})_2O_7$. Rietveld refinements were performed on the four hypothetical models, yielding R_{wp} values of 5.44% (Fig. S2 (a)), 5.33% (Fig. S2 (b)), 5.87% (Fig. S2 (c)), and 5.61% (Fig. S2 (d)), respectively. Notably, all these values exceed 5% and are significantly higher than the R_{wp} obtained for our proposed dual-site $La_{0.500}Y_{0.500}$-HE model (Fig. S1 (f)). This demonstrates that forcing Y^{3+} into a single site fails to accurately capture the experimental lattice parameters and bond length distortions, leading to poor fits of the diffraction profiles.

In addition, thermodynamic stability confirmed by first-principles calculations also fundamentally corroborates our conclusion. We utilized Vienna Ab initio simulation package (VASP) to perform full geometric relaxations and single-point energy calculations for three representative configurations: our proposed dual-site $La_{0.500}Y_{0.500}$-HE, a model with Y^{3+} exclusively at the *A* site ($(La_{0.250}Y_{0.750})_2(Zr_{0.250}Ce_{0.125})_2O_7$), and a model with Y^{3+} exclusively at the *B* site ($(La_{0.500}Ce_{0.125}Sn_{0.125}Nb_{0.250})_2(Zr_{0.250}Y_{0.750})_2O_7$), followed by the calculation of their formation energies (E_{form}):

$$E_{form} = E_{defect} - E_{perfect} - \sum n_i \mu_i + \sum n_j \mu_j \tag{10}$$

Where E_{defect} and $E_{perfect}$ denote the total energies of the doped and pristine systems, respectively, while $n_i\mu_i$ and $n_j\mu_j$ correspond to the sum of the products of the number and chemical potential for the doped and

removed atoms, respectively. The $E_{perfect}$, $n_i\mu_i$ and $n_j\mu_j$ values are identical for all three configurations. The calculated E_{defect} values are -0.7788×10^3 eV (dual-site), -0.7760×10^3 eV (*A*-site only), and -0.7716×10^3 eV (*B*-site only), respectively. The results indicate that the dual-site $La_{0.500}Y_{0.500}$-HE possesses the lowest formation energy, suggesting it is the most thermodynamically stable structure.

In summary, macroscopic peak shifts, microscopic structural refinements and thermodynamic DFT calculations consistently prove the validity of our proposed dual-site occupancy model.

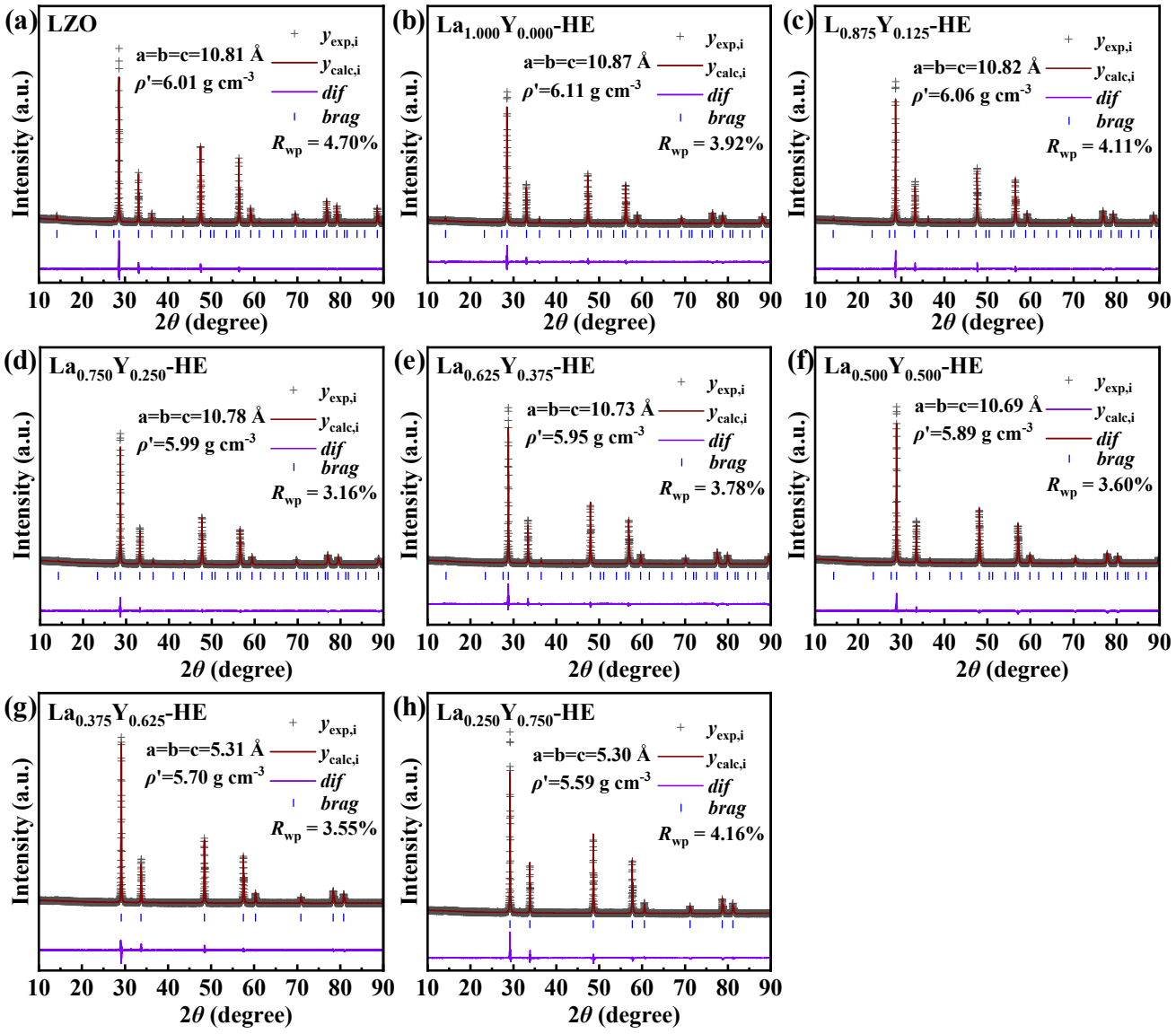

Fig. S1 Rietveld refinement of XRD patterns for (a) LZO, (b-h) $La_{1-x}Y_x$-HE.

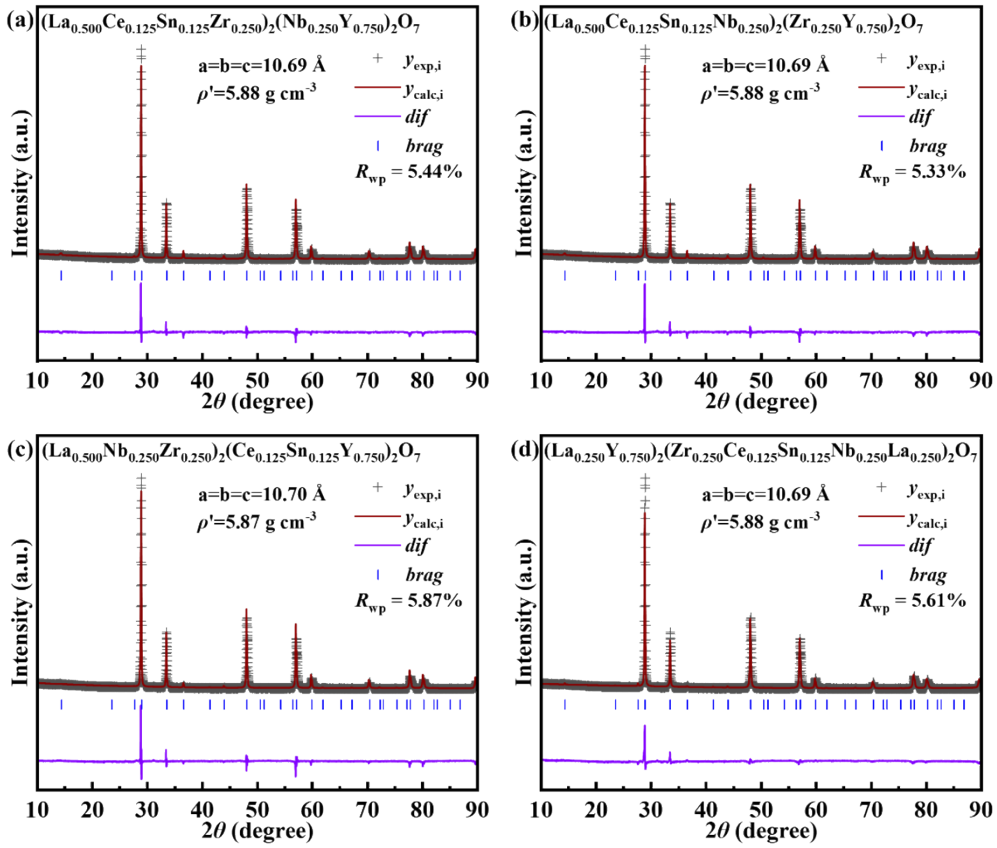

Fig. S2 Rietveld refinement of XRD patterns for (a) $(La_{0.500}Ce_{0.125}Sn_{0.125}Zr_{0.250})_2(Nb_{0.250}Y_{0.750})_2O_7$, (b) $(La_{0.500}Ce_{0.125}$-$Sn_{0.125}Nb_{0.250})_2(Zr_{0.250}Y_{0.250})_2O_7$, (c) $(La_{0.500}Nb_{0.250}Zr_{0.250})_2(Ce_{0.125}$-$Sn_{0.125}Y_{0.750})_2O_7$, (d) $(La_{0.250}Y_{0.750})_2(Zr_{0.250}Ce_{0.125}$-$Sn_{0.125}Nb_{0.250}La_{0.250})_2O_7$.

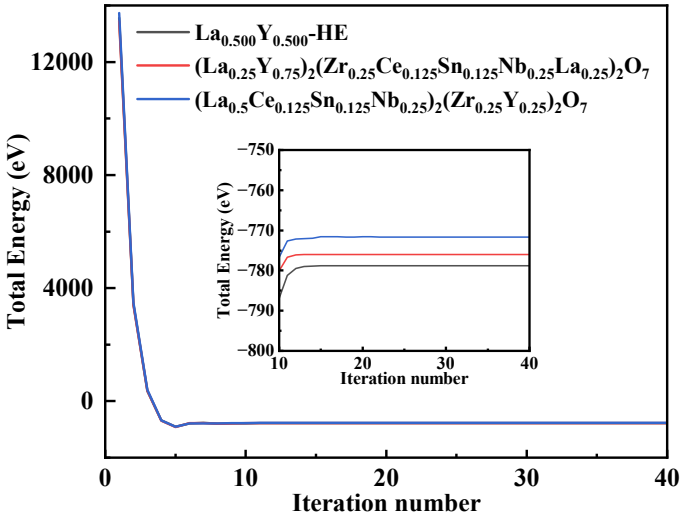

Fig. S3 Comparison of calculated formation energies: $La_{0.500}Y_{0.500}$-HE, $(La_{0.250}Y_{0.750})_2(Zr_{0.250}Ce_{0.125}$-$Sn_{0.125}Nb_{0.250}La_{0.250})_2O_7$ and $(La_{0.500}Ce_{0.125}Sn_{0.125}Nb_{0.250})_2(Zr_{0.250}Y_{0.250})_2O_7$.

3. Numerical simulation and thermal performance analysis

Finite element simulations were performed using COMSOL Multiphysics software to evaluate the thermal response of three different TBCs-based systems: conventional YSZ, LZO, and the $La_{0.500}Y_{0.500}$-HE. As shown in Fig. S4 (a), a two-dimensional axisymmetric geometric model with a total width of 6.40 mm was constructed. Its multilayer structure, from bottom to top, consists of a 1.50 mm nickel-based superalloy, a 0.10 mm bond coat (BC) layer, a 0.01 mm thermally grown oxide (TGO) layer, and a 0.20 mm top TBC layer. The heat transfer within the multilayer TBCs-based systems is governed by the transient heat conduction equations:

$$\rho C_p \frac{\partial T}{\partial t} = \frac{\partial}{\partial x}\left(k \frac{\partial T}{\partial x} \right) \tag{11}$$

$$\frac{\partial T}{\partial t} = a \frac{\partial^2 T}{\partial x^2} \tag{12}$$

$$a = \frac{k}{\rho C_p} \tag{13}$$

The material properties of each layer (including thermal conductivity, specific heat capacity, and density as a function of temperature) are assigned based on experimental data and literatures [S1, S2]. The boundary conditions are set as follows: a constant high temperature of 1773 K is applied to the top surface of the TBCs to simulate the high-temperature gas flow environment; the bottom surface of the superalloy substrate is set to a constant low temperature of 873 K, representing the cooling channel conditions; the sides of the model and the internal pore regions of the TBCs are set as adiabatic boundaries (i.e., zero heat flux density). The initial condition is set to a uniform temperature of 873 K throughout the entire computational domain.

The steady-state temperature distributions and transient thermal responses of the three TBCs-based systems are presented in Fig. S4 (b) and (c), respectively. Although identical boundary conditions were applied, distinct temperature gradients and interfacial temperature drops were observed, attributed to the varying thermophysical properties of the TBCs layers. Notably, the $La_{0.500}Y_{0.500}$-HE based system exhibited the most gradual temperature gradient, indicating superior thermal insulation performance. Quantitatively, its steady-state bottom surface temperature of TBC (T_a) reached only 1106.0 K, significantly lower than that of the LZO (1173.6 K) and conventional YSZ (1234.2 K) systems. More critically, the temperature at the Ni-based superalloy substrate interface was minimized to 1075.8 K in the $La_{0.500}Y_{0.500}$-HE based system, representing a substantial reduction compared to the LZO (1135.2 K) and YSZ (1187.8 K) counterparts. These results suggest that implementing this $La_{0.500}Y_{0.500}$-HE in gas turbine applications could enable higher turbine inlet temperature, significantly extend blade service life, reduce cooling air consumption, and ultimately enhance overall engine efficiency.

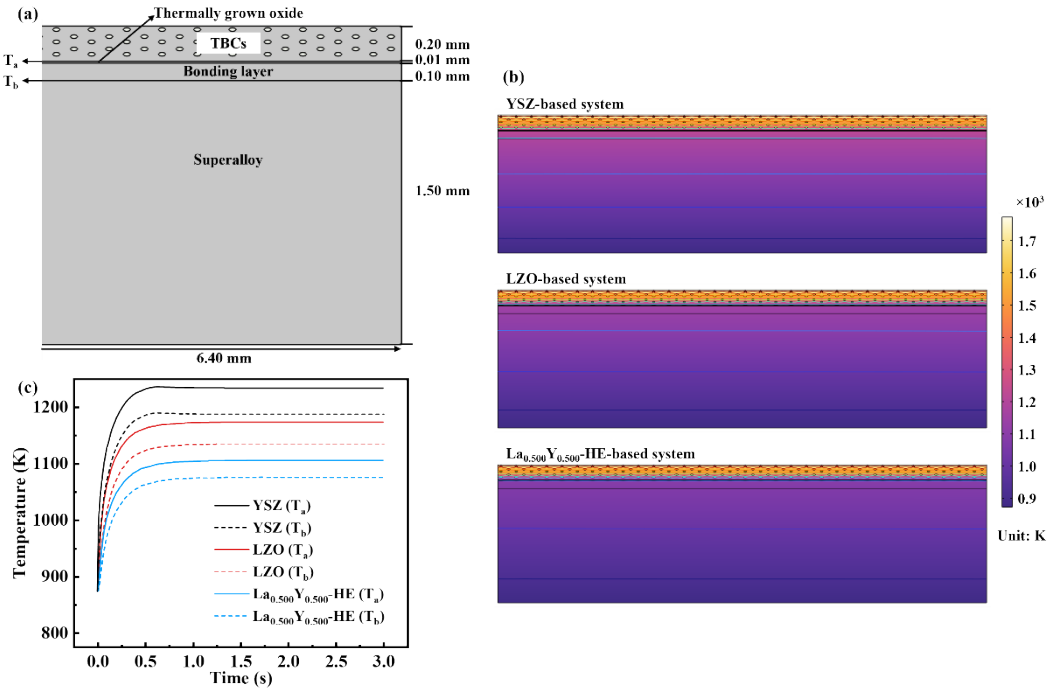

Fig. S4 (a) Model of the TBCs-TGO-BC-Superalloy system used in the finite element simulation; (b) Steady-state temperature distribution contours for three systems; (c) Transient temperature evolution curves at the bottom of the TBCs and the top of the superalloy over time for three systems.

4. TG-DSC and in-situ XRD measurement

The thermal stability of $La_{0.500}Y_{0.500}$-HE was evaluated by thermogravimetry-differential scanning calorimetry (TG-DSC, STA 449, NETZSCH) and in-situ X-ray diffraction (in-situ XRD, D8 Advance, Bruker). TG-DSC measurements were carried out from 300 K to 1300 K at a heating rate of 5 K min^{-1} under a continuous flow of argon as both protective and purge gas. In-situ XRD patterns were collected from 300 K to 1800 K using Cu Kα radiation over a 2θ range of 10° - 90°, with a step size of 0.013° and a scanning rate of 0.0417° s^{-1}, which temperature range covers the typical inlet temperature of gas turbines.

As shown in Fig. S5 (a), the TG-DSC curves of $La_{0.500}Y_{0.500}$-HE exhibit no significant mass loss or endothermic/exothermic peaks from room temperature to 1300 K. Meanwhile, the in-situ XRD patterns show no loss of the superlattice diffraction peaks at approximately 36° and 44° up to 1800 K, indicating no phase transition occurred during heating, as shown in Fig. S5 (b). Above results demonstrate the high-temperature phase stability of the synthesized $La_{0.500}Y_{0.500}$-HE oxides.

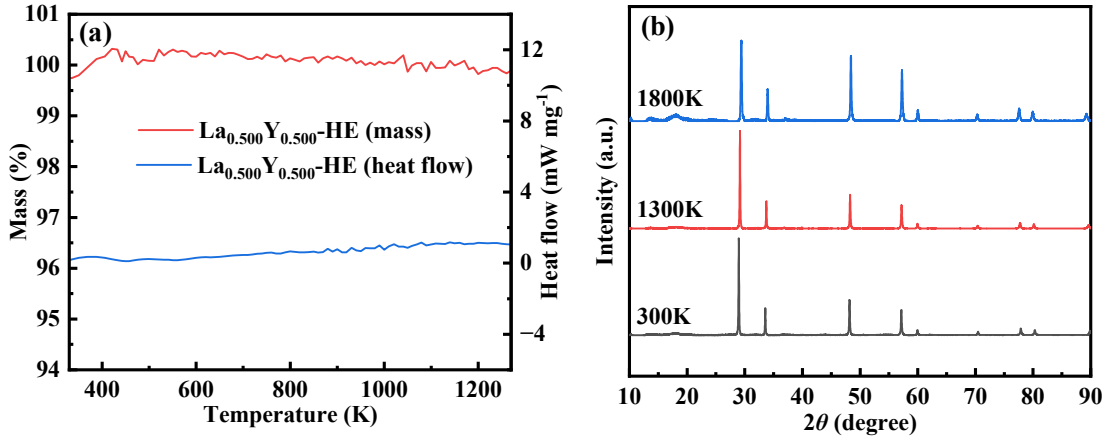

Fig. S5 (a) TG-DSC curves and (b) in-situ XRD patterns of $La_{0.500}Y_{0.500}$-HE.

5. Comprehensive evaluation of TBCs properties

In the field of TBCs materials, the synergistic optimization of comprehensive properties represents the primary objective. As illustrated by the radar chart in Fig. S6, the radar chart clearly illustrates that $La_{0.500}Y_{0.500}$-HE achieves the most balanced and superior overall performance, evidenced by its maximized coverage area relative to commercial YSZ and LZO. While the Vickers hardness and thermal expansion coefficient of $La_{0.500}Y_{0.500}$-HE are slightly lower than those of YSZ, this minor trade-off is offset by its significantly lower thermal conductivity, lower density, and reduced Young's modulus. The reduced Young's modulus is particularly beneficial for enhancing the strain tolerance of the coating, while the ultra-low thermal conductivity addresses the critical need for thermal protection. Thus, this visual representation confirms that $La_{0.500}Y_{0.500}$-HE successfully achieves a balanced optimization of conflicting thermomechanical properties.

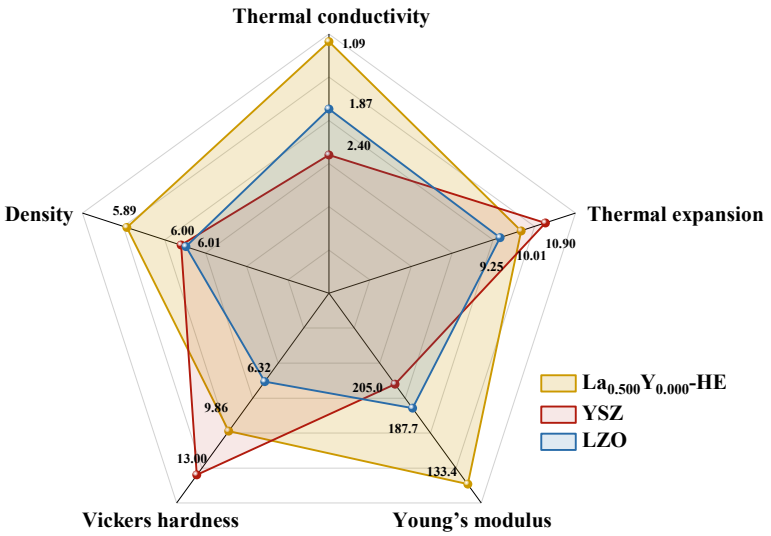

Fig. S6 Radar charts of comprehensive properties for $La_{0.500}Y_{0.500}$-HE, YSZ, and LZO.

Table S1 Nominal and measured atomic percentages of elements in LZO and $La_{0.500}Y_{0.500}$-HE.

Element	LZO		$La_{0.500}Y_{0.500}$-HE	
	Nominal at. %	Measured at. %	Nominal at. %	Nominal at. %
La	60.36	66.33±0.31	32.38	35.38±0.29
Zr	39.64	33.67±0.27	10.63	12.61±0.27
Ce	-	-	8.16	5.37±0.11
Sn	-	-	6.92	4.49±0.06
Nb	-	-	10.83	11.07±0.14
Y	-	-	31.08	31.08±0.30

Table S2 Acoustic velocity of $La_{1-x}Y_x$-HE and LZO.

Compounds	V_L (m s^{-1})	V_T (m s^{-1})	V_M (m s^{-1})

LZO	3511	6484	3918
$La_{1.000}Y_{0.000}$-HE	3416	6303	3812
$La_{0.875}Y_{0.125}$-HE	3404	6243	3797
$La_{0.750}Y_{0.250}$-HE	3416	6144	3805
$La_{0.625}Y_{0.375}$-HE	3224	6114	3605
$La_{0.500}Y_{0.500}$-HE	3020	5574	3370
$La_{0.375}Y_{0.625}$-HE	3144	5631	3501
$La_{0.250}Y_{0.750}$-HE	3297	5727	3661

Table S3 Young's modulus (E), shear modulus (G), bulk modulus (B), Poisson ratio (v), Vickers hardness (H_v), and fracture toughness (K_{IC}) of $La_{1-x}Y_x$-HE and LZO.

Compounds	E (GPa)	G (GPa)	B (GPa)	v	H_v (GPa)	K_{IC} (GPa)
LZO	187.7	72.6	150.9	0.29	6.32	1.98
$La_{1.000}Y_{0.000}$-HE	178.1	68.9	142.7	0.29	9.58	2.15
$La_{0.875}Y_{0.125}$-HE	171.2	66.4	134.9	0.29	9.63	2.35
$La_{0.750}Y_{0.250}$-HE	172.1	67.4	128.2	0.28	9.69	2.56
$La_{0.625}Y_{0.375}$-HE	152.5	58.3	132.0	0.31	9.81	2.45
$La_{0.500}Y_{0.500}$-HE	133.4	51.6	107.0	0.29	9.86	2.46
$La_{0.375}Y_{0.625}$-HE	141.0	55.4	103.7	0.27	9.83	2.36
$La_{0.250}Y_{0.750}$-HE	150.1	59.9	100.9	0.25	9.76	2.47

References

[S1] Gan M, Chong X, Lu T, et al., Unveiling thermal stresses in $RETaO_4$ (RE = Nd, Sm, Eu, Gd, Tb, Dy, Ho and Er) by first-principles calculations and finite element simulations [J]. ***Acta Materilia.*** 2024. 271: 119904.

[S2] Wang L, Wang Y, Sun X, et al., Influence of pores on the thermal insulation behavior of thermal barrier coatings prepared by atmospheric plasma spray [J]. ***Materials and Design.*** 2011. 32: 36-47.